ADVANCED FUNCTIONAL MATERIALS
www.afm-journal.de

High-Resolution, Flexible, and Full-Color Perovskite Image Photodetector via Electrohydrodynamic Printing of Ionic-Liquid-Based Ink

Qilu Wang, Guannan Zhang, Hanyuan Zhang, Yongqing Duan, Zhouping Yin, and YongAn Huang**

Direct full-color image photodetectors without dichroic prisms or sophisticated color filters have considerable advantages in target recognition and information acquisition for electronic eyes and wearable sensors. However, the ability to combine various multispectral semiconductors in a high-resolution and cost-effective manner is still challenging. Here, high-resolution electrohydrodynamic (EHD) printing, together with ionic liquid methylammonium acetate (MAAc) as the solvent, is first introduced to directly integrate various spectral-response perovskite films into a pixelized full-color photodetector. EHD printing enables micro/nanopatterning by using high electrical force to induce jetting, and MAAc improves film quality with scant pinholes and large-size grains by decreasing the perovskite growth rate. By optimizing the printing process and crystallization condition, 1 μm perovskite dot arrays are EHD printed; this is, to the best of knowledge, the smallest printed feature size of perovskite application. And the photodetector still achieves high *R* and *D values of 14.97 A W^{-1} and 1.41×10^{12} Jones, respectively. Finally, an integrated flexible full-color image photodetector is constructed, which successfully realizes light signal detection and color recognition, paving a versatile and competitive approach for future full-color image sensors and artificial vision systems.**

1. Introduction

A lasting surge in the demand for electronic eyes and wearable scanners has inspired the persistent pursuit of high-resolution, flexible, and full-color image photodetector.[1–6] For example, the bionic eyes simulate the composition and function of the human retina, which contains about 100–120 million visual cells with a density of around 0.1 cell μm^{-2},[7] proposing the requirement for high imaging resolution of full-color image sensors. However, traditional image detection systems and most of the recently reported works have to integrate color filters,[8–11] prisms,[12] or optical microcavities,[13,14] which limits the pixel density and flexible application scenarios, and merely responds to specific wavelength range meanwhile loses some spectral information. Consequently, the most ideal way is combining various multispectral, tiny, and high-performance semiconductors on the same substrate to reconstruct precise monochromatic or broadband spectral. Perovskite is an excellent choice in full-color device applications[15–19] due to its ultra-broadband detection, adjustable bandgap, fast response, large detectivity, and solution-process compatibility.[20–22] However, reducing feature pixel size meanwhile guaranteeing the device's optoelectronic performance is a foremost technical challenge, which crucially affects the miniaturization and image quality.

Currently, construction of various absorption spectrum perovskite materials in a high-resolution manner to realize full-color imaging is a hot topic. Two main approaches, i.e., construction of continuous structures with graded bandgap[16,17] and pixelized structures with discrete bandgaps,[15] have been tried to realize full-color imaging. The first one faces problems in large scale, cost-effective, and digitalized manufacturing, and the other extensively researched method has difficulties in patterning of perovskite materials with different bandgaps. Xue et al. used casting method to realize narrow-band response of red, green, and blue light,[15] but the relatively large pixels (1 cm × 1 cm) with considerable thickness (≈20 μm) hindered high-resolution and flexible scenarios applications. Lee and Wu et al. introduced hydrophilic–hydrophobic spin-coating method[23,24] to prepare perovskite array, but this method cannot pattern different materials into one device to realize full-color recognition. Harwell and Cheng utilized photolithography to construct high-resolution red, green, and blue perovskite arrays for photoluminescence devices,[19,25] which was quite complicated and had not to be applied to full-color image photodetectors. Song et al. prepared photodetector arrays employing inkjet printing, which was considered as one of the best patterning methods due to high material utilizing rate, low cost, and compatibility with flexible substrates and various solution parameters.[26,27] However, conventional inkjet printing processes, typically by thermal or piezoelectric actuation, are

Q. Wang, G. Zhang, H. Zhang, Dr. Y. Duan, Prof Z. Yin, Prof Y. Huang
State Key Laboratory of Digital Manufacture Equipment and Technology
Huazhong University of Science and Technology
Wuhan 430074, China
E-mail: duanyongqing@hust.edu.cn; yahuang@hust.edu.cn
The ORCID identification number(s) for the author(s) of this article can be found under https://doi.org/10.1002/adfm.202100857.

DOI: 10.1002/adfm.202100857

challenging in fabricating high-resolution patterns and using highly viscous materials. At present, flexible, high-resolution, and full-color perovskite image photodetectors are rarely reported.

Here, we first exploited high-resolution EHD printing technology,[28,29] together with high-viscosity and environmentally friendly ionic liquid methylammonium acetate (MAAc) as a solvent, to fabricate high resolution, flexible and full-color perovskite image photodetector. EHD printing utilizes high electrical force to deform the pendent drop at the nozzle tip into a Taylor cone, from which a micro/nanojet is pulled out to generate extremely small droplets and patterns, and MAAc can stabilize the high-resolution drop-on-demand printing process in air without using anti-solvent. More importantly, thanks to the negligible vapor pressure of MAAc, it can remain in the printed film under a comparatively high temperature. In this case, a quick liquid-to-solid transition through a new perovskite intermediate structure greatly delays the growth rate of perovskite crystals, facilitating the uniform nucleation and crystal growth. High-resolution dot arrays of 1 μm have been successfully achieved through EHD printing. By patterning different bandgap perovskite materials into micro subpixels, optimizing the annealing process to improve crystallization, and using the strong band-edge absorption and cutoff edge wavelength difference to identify color, full-color imaging sensor was fabricated, successfully mapping light source signals and recognizing colors.

2. Results and Discussion

Inspired by human eyes, we designed a flexible full-color perovskite image photodetector, which can act as electronic eyes in the foreseeable future, as shown in **Figure 1**a. The overall structure of the device was schematically illustrated in Figure 1b, and the device was composed of row electrodes (Cr and Au), insulation blocks, column electrodes (Au) and perovskite arrays, where the last layer was prepared by EHD printing. Figure 1c shows a process schematic diagram from printing to in situ precrystallization to postannealing, further forming high-quality perovskite films. In detail, by attaching a high pulse voltage between the glass nozzle and the grounded substrate, the pendent drop at the end of the nozzle first transformed into a Taylor cone, then emitted a thin slender jet from the apex and formed droplets on substrate when the electrostatic stress overcame the surface tension of the meniscus. A prerequisite for enabling stable drop-on-demand printing is preparing inks with good stability and reliable processability in air. However, traditional perovskite solvents such as DMF and DMSO face two rigorous problems in printing: i) the toxic solvents are extremely unsuitable for printing directly in air; ii) tiny droplets are easier to have more pinholes and crystal defects due to the excessive evaporation and insufficient time to flow and crystallize compared to large droplets. The precursor inks of discrete bandgaps used here for EHD printing were prepared by adding methylammonium halide and lead halide into ionic liquid solvent MAAc, which helped to stabilize the drop-on-demand printing process meanwhile ensuring film performance printed in air without using antisolvent.[30–32]

Various perovskite physical properties such as color, absorption spectrum, and photoluminescence (PL) spectrum can be tuned by varying the halide composite (Cl, Br, and I), as shown in **Figure 2**a–c. When varying the halide ion from Cl^- to Br^- and to I^-, the color of $MAPbX_3$ inks changed from transparency to yellow. Figure 2b shows the absorption spectra of the

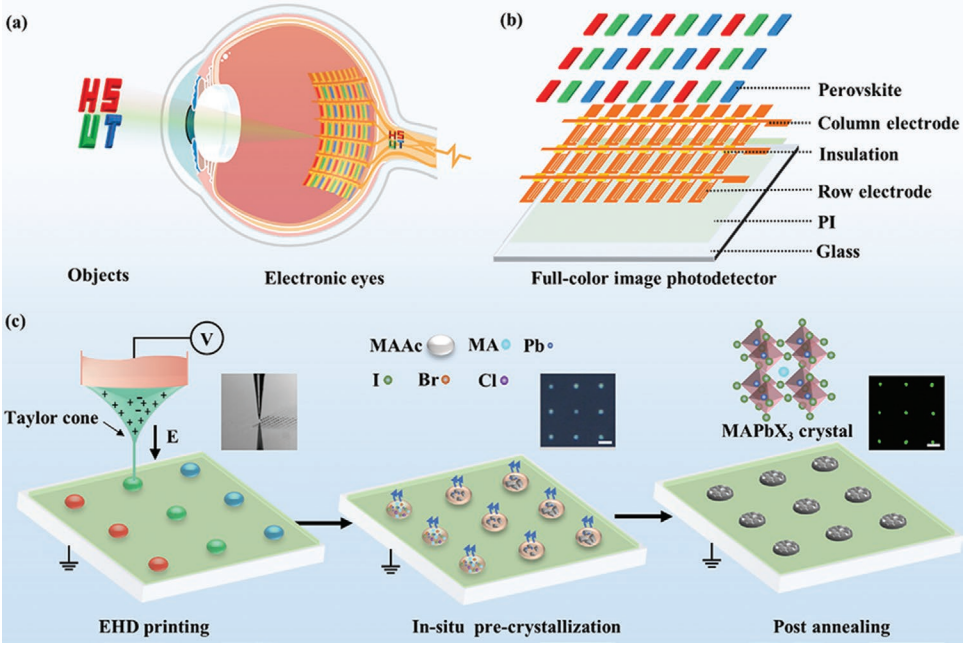

Figure 1. a) Flexible full-color image photodetectors acting as electronic eyes in the artificial visual system. b) Schematic illustration of layer by layer structure of full-color perovskite image photodetector. c) Schematic illustration of the EHD printing fabrication process and perovskite transformation from $MAPbX_3$ ink to polycrystalline film. The inserts are observation microscope image, microphotograph of the EHD printed perovskite microarray, and fluorescent picture of the EHD printed perovskite microarray from left to right, respectively. The scale bar is 5 μm.

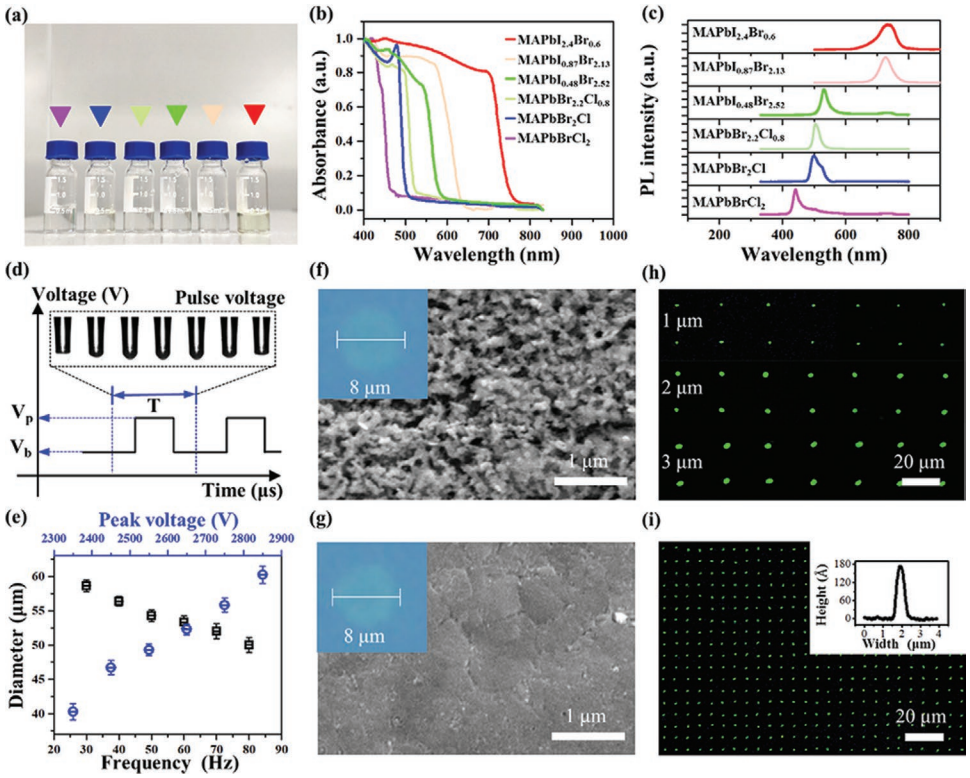

Figure 2. a) Photographs of the solution of $MAPbX_3$ inks. b,c) Normalized absorption spectra and normalized PL spectra of $MAPbBrCl_2$, $MAPbBr_2Cl$, $MAPbBr_{2.2}I_{0.8}$, $MAPbI_{0.48}Br_{2.52}$, $MAPbI_{0.87}Br_{2.13,}$ and $MAPbI_{2.4}Br_{0.6}$ films. d) Pulse voltage used in EHD printing. V_p and V_b denote the peak and baseline voltage, respectively. The insert image shows the shape of the solution at the nozzle tip changes in sequence within one cycle. e) $MAPbX_3$ dot diameter versus pulse frequency and peak voltage. The nozzle diameter, V_p and V_b are fixed at 30 μm, 2450 V, 1900 V and the nozzle diameter, V_b, and pluse frequency are fixed at 30 μm, 1900 V, 60 Hz at two different experiments, respectively. f,g) SEM images of printed $MAPbI_{2.4}Br_{0.6}$ films by using inks with different solvents (DMF and MAAc). The inserts are microphotographs of the printed perovskite dot. h) The EHD printed high-resolution dot array with dot diameter of 1, 2, and 3 μm respectively. i) The EHD printed high-resolution dot array with diameter of ≈1 μm, and the insert is height profile of one single perovskite dot.

$MAPbX_3$ films, and one can observe that the absorption cutoff wavelength could be effectively tuned in the range from 440 to 740 nm, showing apparently strong band-edge absorption, making it possible to realize color recognition. Figure 2c shows PL spectra of the $MAPbX_3$ films, and the PL peak shifted to a higher energy direction as the I^- content increasing.

Apart from the aforementioned ink design, precise control of EHD printing process is also vital for stable drop-on-demand printing and high-resolution patterning. As shown in Figure 2d, a pulse voltage was utilized in EHD printing, where the peak voltage (V_p) was chosen to induce a jetting mode for a short duration and the baseline voltage (V_b) should ensure an interrupt of jetting. With the increase of peak voltage, the average dot diameter linearly increased as a higher peak voltage due to a larger electric force applied to the ink meniscus, thus more ink was pulled down to the substrate. Meanwhile, the average dot diameter decreased with the pulse frequency, considering that higher pulse frequency corresponds to shorter jetting time and smaller droplet size (Figure 2e and Figure S1, Supporting Information). By regulating the pulse voltage and printing distance to accommodate the perovskite ink properties, the drop generation frequency was always equal to the pulse voltage frequency (f=1/T) to ensure precisely drop-on-demand printing (Figure S2, Supporting Information). In Figure 2f,g, the insert SEM images showed two different morphologies of perovskite crystals formed by using inks with different solvents (DMF and MAAc). After EHD printing on a heated substrate, the DMF-based droplet scattered like isolated islands that the perovskite crystallites did not connect with each other well, with more pinholes and defects owing to the fast solvent evaporation and lack of sufficient time to crystallize. Contrary to DMF, uniform and high coverage films based on MAAc were formed, attributed to the extremely low vapor pressure of MAAc, which greatly delayed the growth rate of perovskite crystals and facilitated the uniform nucleation and crystal growth. The result proved that the perovskite crystallite morphology relies heavily on the solvent and MAAc was an optimal solvent for the EHD printing. Besides the above parameters, nozzle diameter is another decisive factor for droplet size, and a smaller nozzle diameter helps to get a smaller droplet size. A glass capillary nozzle with an inner diameter of 8 μm was used to print high-resolution dot array. When two adjacent dots were close enough, they could be merged into a line array. Dot and line arrays could be efficiently created as shown in Figure S3 (Supporting Information). By exploiting the rules described above between droplet diameter and various parameters, we can adjust droplet size

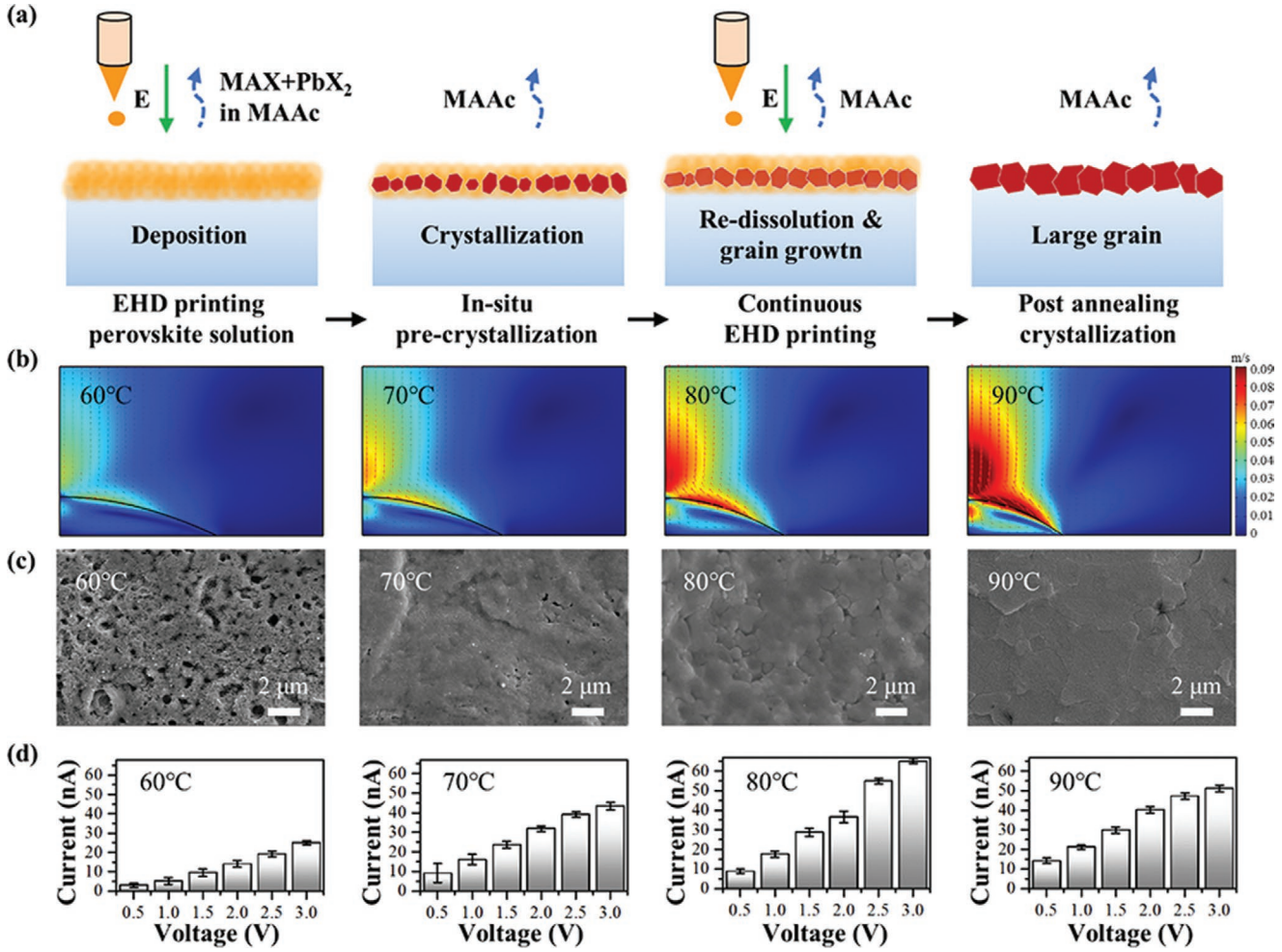

Figure 3. a) Schematic illustration of the mechanism of the whole EHD printing and crystallization process. b) Finite element simulation results of droplet evaporation at different substrate temperatures. c) SEM images of $MAPbI_{2.4}Br_{0.6}$ films formed at different substrate temperatures. d) *I–V* characteristics of individual pixel device prepared at different substrate temperatures.

precisely as shown in Figure 2h,i. Then we further studied the morphology evolution of perovskite dots with various sizes in Figure S4 (Supporting Information), and found that smaller droplet films preferred more uniform films. Finally, a perovskite dot array with a minimal diameter of ≈1 μm and thickness of ≈18 nm was fabricated, whose resolution was 5080 dpi approximately. This is, to the best of our knowledge, the smallest printed feature size in the perovskite application.

We further adjusted in situ crystallization temperature during EHD printing process to acquire high-quality perovskite films with more surface coverage and fewer defects, enabling good performance of device. The process that $MAPbX_3$ precursor ink transformed into $MAPbX_3$ polycrystalline film onto substrate was illustrated in **Figure 3**a. Precursor ink was first printed onto a hot substrate, and the substrate with perovskite films was then annealed at 100 °C for 10 min to complete crystallization after printing. Perovskite film formation is a combination process of nucleation and crystal growth, where the crystal nucleation rate v_1, crystal growth rate v_2, and the number of grains per unit area N (inversely proportional to the grain size) are determined as a function of the supersaturation degree σ by the following equations:[33–35]

$$v_1 \propto e^{-\frac{1}{\sigma^2}} \tag{1}$$

$$v_2 \propto \sigma^2 \tag{2}$$

$$N = 1.1\left(\frac{v_1}{v_2}\right)^{\frac{1}{2}} \tag{3}$$

The competition between v_1 and v_2 decides the grain size and whether inherent defects such as rich pinholes occur. As expressed by the formulas, within a certain temperature range, supersaturation increases with temperature, and the growth rate is greater than the nucleation rate, contributing to the formation of large grains. However, if the temperature is too high, the nucleation rate will be greater than the growth rate and lead to small grain defects. In order to further study the mechanism of fluid flow and evaporation at different temperatures, a finite element model was established to simulate film formation of

perovskite ink on the hot substrate. By solving Navier–Stokes equations, heat transfer equations, and mass diffusion equations,[36,37] the results presented in Figure 3b, Figures S5 and S6 (Supporting Information) show that, with the increase of temperature, the difference between the evaporation rate at the edge and that in the middle of the droplet increased, causing the intermediate solution to flow to the edge to form a capillary flow. According to the calculation results, the Marangoni flow was at a disadvantage in the competition with the capillary flow, which was not conducive to the formation of a uniform film. Therefore, the substrate temperature should be within an appropriate range.

To explore the best in situ precrystallization temperature, four representative samples set at different temperatures were analyzed, and their top-view SEM images were shown in Figure 3c. The films prepared at higher temperature exhibited larger domain sizes in the range of 60 °C to 90 °C. But some cracks appeared causing by precrystallization temperature higher than the perovskite crystallization temperature at 90 °C. It was worth noting that high dense film with large crystal grains and scant pinholes was obtained at the temperature of 80 °C in Figure S7 (Supporting Information), which was a better choice for photodetectors. Figure 3d showed the *I–V* characteristics of photodetectors prepared at different substrate temperatures. The photodetectors fabricated at 80 °C showed the best device performance due to low defects and high surface coverage as expected.

Figure 4a showed the final device of full-color image photodetector utilizing Au–perovskite–Au photoconductor structure and its energy band illustration. As shown in Figure 4b,c, the device with 10 × 10 pixels (10 × 10 × 3 subpixels) was designed and fabricated on a glass substrate. The detailed structural parameters were shown in Figures S8 and S9 (Supporting Information). Figure 4d and Figure S10 (Supporting Information) presented *I–V* characteristics of the individual pixel under dark and illumination by using different light sources with increasing light intensity. The current increased with the light intensity due to much more electron–hole pairs generated. Some *I–V* curves exhibited different linearities, which may be influenced by the undesired interface states at the perovskite/Au interface because of some accidental factors like the wettability state of the substrate, humidity, and so on. Figure 4e presents the response of the device to 530 nm illumination with switching "ON" and "OFF" states. The measured photocurrent was increased from 317.4 pA in the dark to about 66.0 nA under illumination at +3 V. The response and recovery time were calculated as 65.0 and 68.2 ms at 1 mW cm^{-2}. To further evaluate the devices, the detectivity (D^*), on–off ratio, and responsivity (R) of the device under different light intensities were calculated from the statistics of 10 devices as illustrated in Figure 4f and Figure S11 (Supporting Information), using the following equations:[38] $R = (I_p - I_d)/\mathrm{PS}$ and $D^* = (I_p - I_d)/P(2qI_dS)^{1/2}$, where I_p was the photocurrent, I_d was the dark current, P denoted light power density, and S denoted the device area, q represented elementary charge.

Specifically, our method can be used to fabricate ultrahigh-resolution devices. A photodetector using a ≈5 µm printed droplet with 2 µm channel length was displayed in **Figure 5**a, and its *I–V* characteristics under dark and illumination by using a 530 nm light source was shown in Figure 5b. This photodetector exhibited a R and D^* value of 14.97 A W^{-1} and 1.41 × 10^{12} Jones (light intensity = 0.1 mW cm^{-2}, +3 V applied

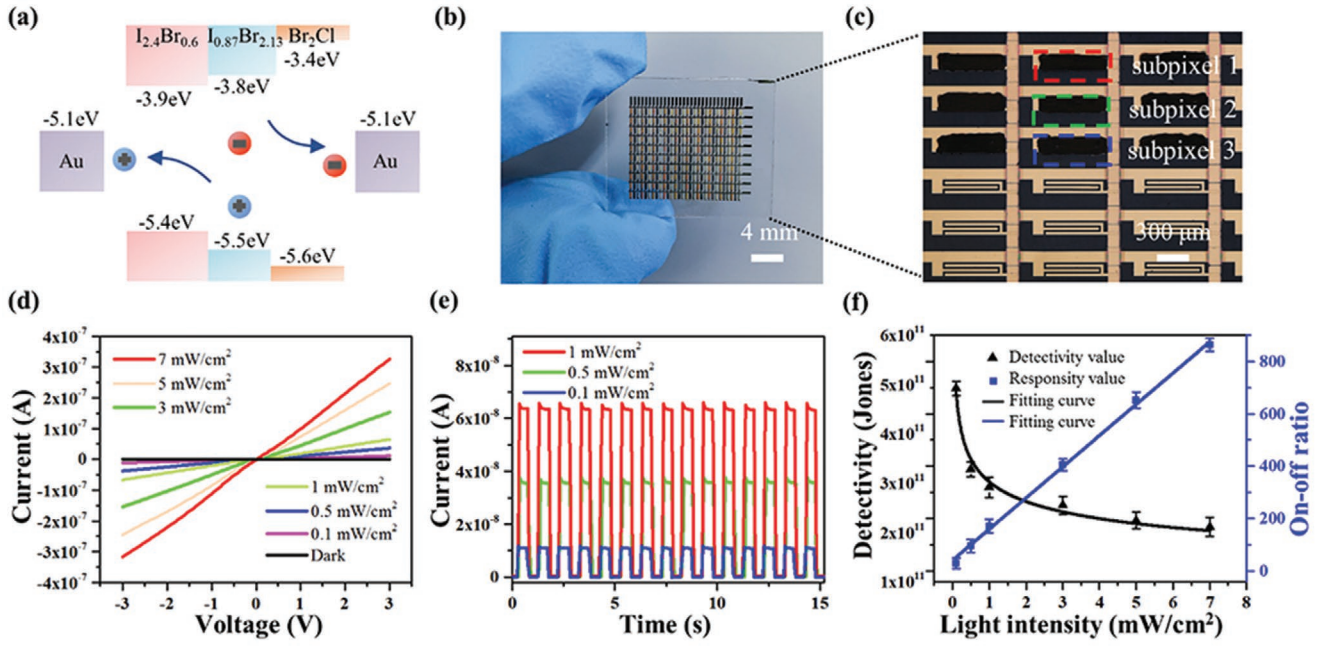

Figure 4. a) Energy band illustration of the device. b,c) Photographs of perovskite image photodetector on a glass substrate. The glass substrate has been patterned with a thin film of chromium (10 nm) and gold (90 nm), SU8 (650 nm), gold (80 nm), and perovskite (4.4 µm). d) *I–V* characteristics of individual $MAPbI_{2.4}Br_{0.6}$ pixel under dark and illumination by using a 530 nm light source with increasing light intensity. e) The transient photocurrent of the device under repeated on/off illumination. f) The detectivity and on–off ratio under different illumination intensities.

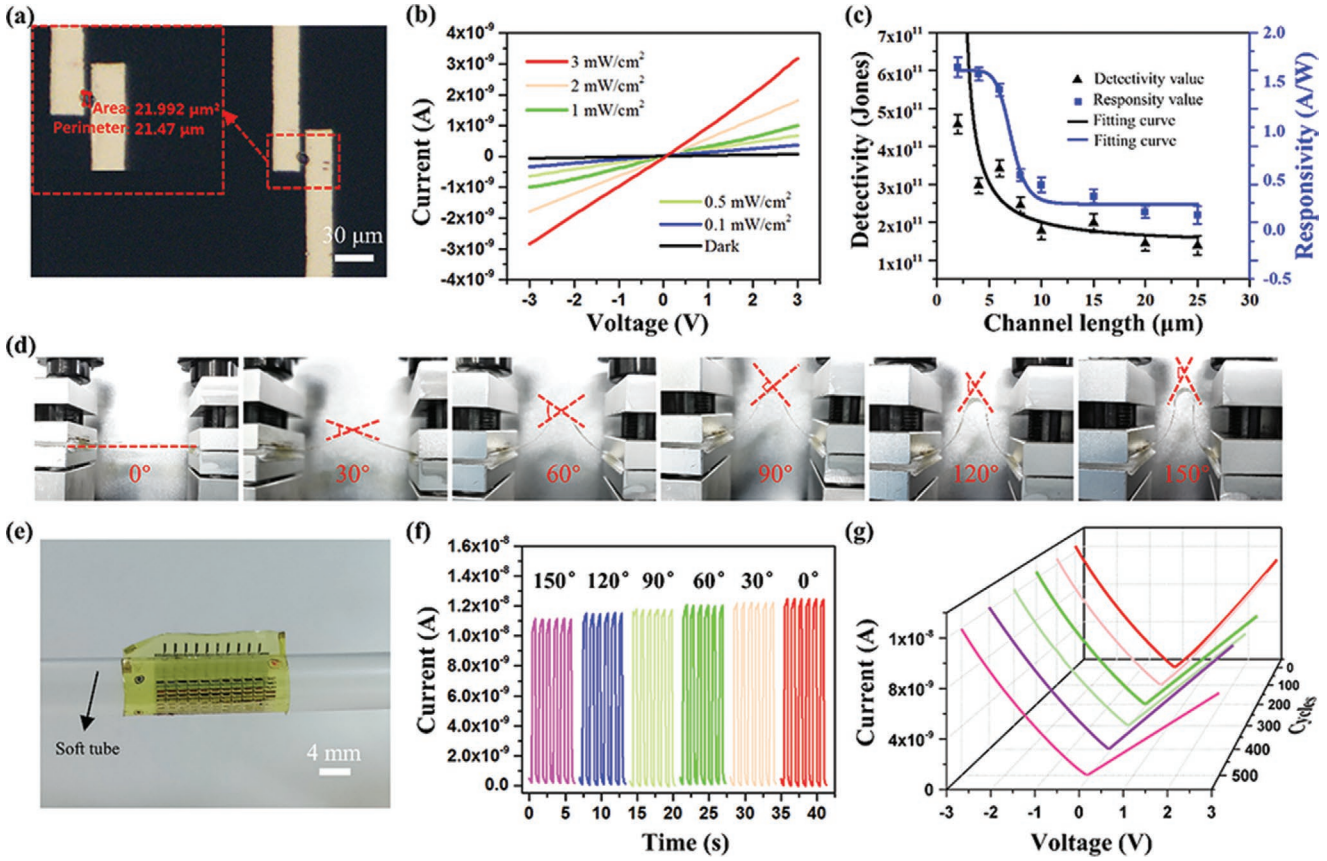

Figure 5. a) Optical photograph of the photodetector employing a 5 μm droplet. The insert is an optical photograph of the channel area covered by perovskite droplet. b) *I–V* characteristics of photodetector employed 5 μm $MAPbI_{2.4}Br_{0.6}$ droplet with 2 μm channel length under dark and different intensities of green light. c) The detectivity and responsivity of photodetectors with various channel lengths under 1 mW cm^{-2} of green light. d) Photographs of the bent photodetector at varied angles from 0° to 150°. e) Optical photographs of flexible image photodetector. f) The photoresponse curves at different bending angles (0.1 mW cm^{-2}, green light). g) Logarithm *I–V* curves of the device without bending and after 100, 200, 300, 400, and 500 bending cycles.

bias voltage), respectively. To the best of our knowledge, this is the smallest printed perovskite photodetector. Furthermore, it was calculated that a resolution of 3175 dpi could be achieved with the 2 μm gold electrode width, 2 μm channel length, 6 μm channel width, and 2 μm pixel interval space as shown in Figure S12 (Supporting Information). Photodetectors with different channel lengths (2–25 μm) and the same channel width (30 μm) was designed, and the *D** and *R* of photodetectors with various channel lengths under the same green light intensity of 1 mW cm^{-2} were depicted in Figure 5c and Figure S11 (Supporting Information), it showed that in a certain range, smaller channel length corresponded to better performance. Moreover, a mechanically flexible full-color image photodetector (≈12 μm thickness) was fabricated, which proved its prospect toward the next-generation wearable full-color image sensor. The bending capability of wearable application was extremely important for the device performance, service life, and application scenarios. So we did some bending tests to clarify the performance of the device under different conditions. As shown in Figure 5d and Figure S13 (Supporting Information), the flexibility of the device under varied angles was tested, and the optical image of flexible photodetector was shown in Figure 5e. The photocurrent evolution after bending 300 times at various angle (0° to 150°) was shown in Figure 5f, even if the photodetector was bent at a large angle (150°), the photocurrent had an acceptable decrease of ~8%. Furthermore, as illustrated in Figure 5g, logarithm *I–V* curves of the flexible photodetector after different bending cycles (100 times to 500 times) at fixed angle (60°) were tested. There was just a slight decrease in the photocurrent after 500 times bending, possibly owing to the small cracks of perovskite film after bending, proving that the photodetector possessed a good mechanical flexibility and electrical stability.

For better verification of the color recognition function and capability, photodetectors based on $MAPbI_{2.4}Br_{0.6}$, $MAPbI_{0.87}Br_{2.13}$, and $MAPbBr_2Cl$ were measured under different light sources with wavelengths of 470, 530, and 680 nm (blue, green, and red light), and they are labeled as subpixel 1, subpixel 2, and subpixel 3, respectively. The logarithm *I–V* curves under illuminations of various wavelength and dark condition were shown in **Figure 6**a–c. As expected, subpixel 3 only responded to the blue light, subpixel 2 responded to both blue and green light, while subpixel 1 responded to three light sources, which were associated with the engineered specific absorption spectra of the perovskite at corresponding positions. The final full-color image photodetector system based on pixelized perovskite absorbers with discrete bandgaps was shown

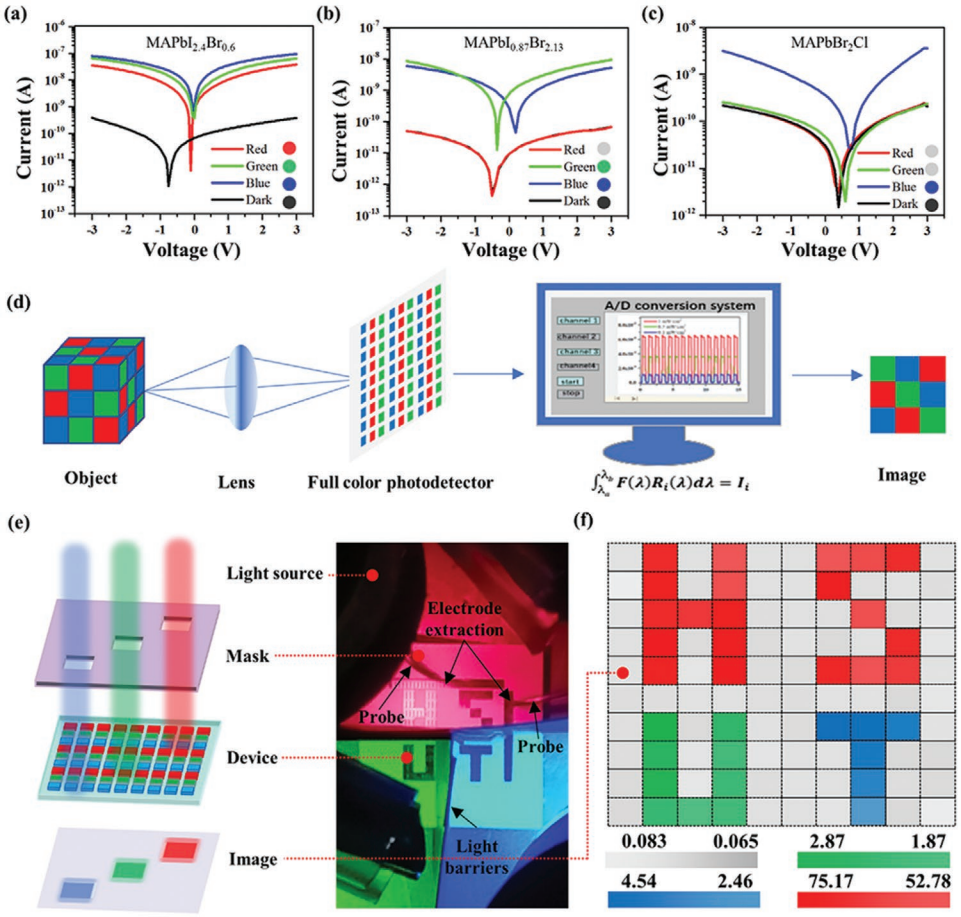

Figure 6. a–c) Logarithm *I–V* curves of photodetectors based on a) $MAPbI_{2.4}Br_{0.6}$, b) $MAPbI_{0.87}Br_{2.13}$, and c) $MAPbBr_2Cl$ under blue, green, and red illuminations. d) Schematic illustration of full-color image photodetector system. e) Schematic illustration and equipment photograph of the image photodetector array to detect light distribution. f) Normalized current mapping result by the full-color image photodetector after patterned illumination through a shadow mask. Numerical units are nA.

in Figure 6d. The principle of color recognition was shown in below formula:

$$\int_{\lambda_a}^{\lambda_b} F(\lambda) R_i(\lambda) d\lambda = I_i \quad (4)$$

where $F(\lambda)$ was the unknown visible light; I_i was the measured photocurrent; $R_i(\lambda)$ was the response function of each subpixel; and λ_a and λ_b defined the device's operational wavelength range. To present device applications, the image photodetector based on subpixel 1, subpixel 2, and subpixel 3 was integrated as one device, which successfully captured an image projected through a shadow-mask and identified the set light source color. As shown in Figure 6e and Figure S14 (Supporting Information), a predesigned shadow mask was placed between the light source and the device to form a colorful "HUST" pattern. As shown in Figure 6f, the pixels exposed to illumination, had higher current values, while others that were blocked by the designed mask had no obvious change in current. A clear pattern "HUST" could be shown in the current mapping results, which indicated the excellent imaging performance of full-color image photodetector. It has great potential in electronic eyes, wearable sensors, and optical communication applications, and integrated manufacture and device performance can be improved ulteriorly for the next generation optoelectronics.

3. Conclusions

This work employed EHD printing and MAAc-based ink to enable facile, fast, and high-resolution patterning of perovskite films, meanwhile ensuring the printed film quality. By optimizing the printing and annealing condition, an extremely high-resolution perovskite dot array of 1 µm (5070 dpi) was directly printed and in-situ crystalized in air, and a smallest printed photodetector exhibited high R and D^* values of 14.97 A W^{-1} and 1.41×10^{12} Jones, respectively. The sensor printed on PI substrate showed superior flexibility which could stand 500 times bending under wide angle (0°–150°) with slight performance decrease. And clear current mapping results demonstrated its excellent full-color imaging performance. The current work provided a versatile tool for fabrication of high-resolution multiplexed perovskite optoelectronic device array for future flexible full-color image sensors and artificial vision applications.

4. Experimental Section

The Materials of the Device: Lead chloride ($PbCl_2$, 99.9%), lead bromide ($PbBr_2$, 99.9%), lead iodide (PbI_2, 99.9%), methylammonium iodide (MAI, 99.9%), methylammonium chloride (MACl, 99.9%), methylammonium bromide (MABr, 99.9%), methylammonium acetate (MAAc) were purchased from Xi'an polymer light technology corp. All reagents were used without further purification.

The Fabrication of the Electrodes: The glass was ultrasonically cleaned with acetone, isopropyl alcohol, ethanol, and deionized water for 15 min each and then dried with nitrogen. Electrodes were fabricated through UV lithography technique Lithography machine (ABM/6/350/NUUV/DCCD/BSV/M), metal deposition, and lift-off process. Specifically, Cr/Au row electrodes with thicknesses of 10 nm/90 nm were deposited by vacuum evaporating. Next, SU8 2000.5 photoresist was spin-coated onto the above substrates at 500 rpm for 8 s and 3000 rpm for 30 s, then baked at 95 °C for 1 min as the insulating layer. By exposure and development, the SU8 film was wiped off except every intersection region of the two vertical cross line electrodes. At last, Au column electrodes were deposited by vacuum evaporating again using a mask. The flexible device was obtained by spin coating polyimide (PI) on a glass substrate, and other steps were the same as mentioned above, and stripped the PI from glass by using a laser lift-off technique at last.

The Jetting Process: The perovskite inks (0.58 mol L^{-1}) were obtained by mixing MABr (MACl, MAI) and $PbBr_2$ ($PbCl_2$, PbI_2) in MAAc at 80 °C for 4 h with constant stirring. The perovskite ink (0.2 mol L^{-1}) with solvent DMF was obtained by mixing MABr, MAI, and PbI_2 in DMF at 80 °C for 4 h with constant stirring. The perovskite ink was supplied to a metal wire inserted glass capillary, then it was fixed onto a motion stage. The printing process was accomplished by applying a high voltage between the nozzle and the substrate at a standoff height of about 30–100 µm. During printing, the substrate was heated at 80 °C to accelerate in situ crystallization. After printing, the substrate with perovskite pattern was annealed at 100 °C for 10 min to complete crystallization. All printing and annealing were done in ambient conditions. A high-resolution EHD printer (EHD Jet-H professional type, Guangdong Sygole Intelligent Technology Co. Ltd.) was used to print solutions. The jetting process was visualized by a high-speed camera (Dimax HD, PCO AG, Germany) with a zoom lens (magnification 1.16–13.92, Navitar Inc., USA).

Photoresponse Characterization: The electrical measurements were performed using two digital source-meter (Keithley 2400) combined with a probe table. During the measurements, LEDs (M470L4, M530L4, M680L4, Thorlabs) modulated by its controller (DC 4100, Thorlabs) were used as light sources. The film surface was measured by field emission scanning electron microscopy (FE-SEM, FEI NOVA NanoSEM 450). UV-vis spectrophotometer (Shimadzu, SolidSpec-3700 using integrating sphere) was applied to study the optical absorption of perovskite film. Photoluminescence (PL) spectra were collected using excitation of wavelength 365 and 540 nm, and the PL images of the printed microarrays were characterized by a fluorescent microscope (Nikon eclipse Ts2R).

Supporting Information

Supporting Information is available from the Wiley Online Library or from the author.

Acknowledgements

Q.W. and G.Z. contributed equally to this work. This work was financially supported by the National Key Research and Development Program of China (2018YFA0703200), the National Natural Science Foundation of China (52075209, 11932009), and the Natural Science Foundation of HuBei Province (2020CFA028). The authors would also like to thank Flexible Electronics Manufacturing Laboratory in Comprehensive Experiment Center for advanced manufacturing and equipment technology.

Conflict of Interest

The authors declare no conflict of interest.

Data Availability Statement

Research data are not shared.

Keywords

electrohydrodynamic printing, full color image sensors, high resolution patterning, image photodetector, perovskite

Received: January 26, 2021
Revised: March 4, 2021
Published online:

[1] S. Seo, S. H. Jo, S. Kim, J. Shim, S. Oh, J. H. Kim, K. Heo, J. W. Choi, C. Choi, S. Oh, D. Kuzum, H. P. Wong, J. H. Park, *Nat. Commun.* **2018**, *9*, 5106.
[2] Y. Lee, J. Y. Oh, W. Xu, O. Kim, T. R. Kim, J. Kang, Y. Kim, D. Son, J. B. Tok, M. J. Park, Z. Bao, T. W. Lee, *Sci. Adv.* **2018**, *4*, eaat7387.
[3] T. Yokota, P. Zalar, M. Kaltenbrunner, H. Jinno, N. Matsuhisa, H. Kitanosako, Y. Tachibana, W. Yukita, M. Koizumi, T. Someya, *Sci. Adv.* **2016**, *2*, e1501856.
[4] S. Goossens, G. Navickaite, C. Monasterio, S. Gupta, J. J. Piqueras, R. Pérez, G. Burwell, I. Nikitskiy, T. Lasanta, T. Galán, E. Puma, A. Centeno, A. Pesquera, A. Zurutuza, G. Konstantatos, F. Koppens, *Nat. Photonics* **2017**, *11*, 366.
[5] R. D. Jansen-van Vuuren, A. Armin, A. K. Pandey, P. L. Burn, P. Meredith, *Adv. Mater.* **2016**, *28*, 4766.
[6] X. Tang, M. M. Ackerman, M. Chen, P. Guyot-sionnest, *Nat. Photonics* **2019**, *13*, 277.
[7] L. Gu, S. Poddar, Y. Lin, Z. Long, D. Zhang, Q. Zhang, L. Shu, X. Qiu, M. Kam, A. Javey, Z. Fan, *Nature* **2020**, *581*, 278.
[8] C. Liu, Q. Zhang, D. Wang, G. Zhao, X. Cai, L. Li, H. Ding, K. Zhang, H. Wang, D. Kong, L. Yin, L. Liu, G. Zou, L. Zhao, X. Sheng, *Adv. Opt. Mater.* **2018**, *6*, 1800146.
[9] W. L. Tsai, C. Y. Chen, Y. T. Wen, L. Yang, Y. L. Cheng, H. W. Lin, *Adv. Mater.* **2019**, *31*, 1900231.
[10] P. Wang, S. Liu, W. Luo, H. Fang, F. Gong, N. Guo, Z. G. Chen, J. Zou, Y. Huang, X. Zhou, J. Wang, X. Chen, W. Lu, F. Xiu, W. Hu, *Adv. Mater.* **2017**, *29*, 1604439.
[11] N. Amraish, A. Reisinger, D. H. Pahr, *Appl. Mech.* **2020**, *1*, 174.
[12] D. Komisarek, K. Reichard, D. Merdes, D. Lysak, P. Lam, S. Wu, S. Yin, *Appl. Opt.* **2004**, *43*, 3983.
[13] A. Sobhani, M. W. Knight, Y. Wang, B. Zheng, N. S. King, L. V. Brown, Z. Fang, P. Nordlander, N. J. Halas, *Nat. Commun.* **2013**, *4*, 1643.
[14] B. Y. Zheng, Y. Wang, P. Nordlander, N. J. Halas, *Adv. Mater.* **2014**, *26*, 6318.
[15] J. Xue, Z. Zhu, X. Xu, Y. Gu, S. Wang, L. Xu, Y. Zou, J. Song, H. Zeng, Q. Chen, *Nano Lett.* **2018**, *18*, 7628.
[16] Z. Yang, T. Albrow-Owen, H. Cui, J. Alexander-Webber, F. Gu, X. Wang, T. C. Wu, M. Zhuge, C. Williams, P. Wang, A. V. Zayats, W. Cai, L. Dai, S. Hofmann, M. Overend, L. Tong, Q. Yang, Z. Sun, T. Hasan, *Science* **2019**, *365*, 1017.

[17] H. Sun, W. Tian, X. Wang, K. Deng, J. Xiong, L. Li, *Adv. Mater.* **2020**, *32*, 1908108.
[18] M. Zhu, Y. Duan, N. Liu, H. Li, J. Li, P. Du, Z. Tan, G. Niu, L. Gao, Y. Huang, Z. Yin, J. Tang, *Adv. Funct. Mater.* **2019**, *29*, 1903294.
[19] J. Harwell, J. Burch, A. Fikouras, M. C. Gather, A. Di Falco, I. D. W. Samuel, *ACS Nano* **2019**, *13*, 3823.
[20] S. D. Stranks, G. E. Eperon, G. Grancini, C. Menelaou, M. J. P. Alcocer, T. Leijtens, L. M. Herz, A. Petrozza, H. J. Snaith, *Science* **2013**, *342*, 341.
[21] G. C. Xing, N. Mathews, S. Y. Sun, S. S. Lim, Y. M. Lam, M. Gra ¨tzel, S. Mhaisalkar, T. C. Sum, *Science* **2013**, *342*, 344.
[22] J. P. Correa-Baena, M. Saliba, T. Buonassisi, M. Grätzel, A. Abate, W. Tress, A. Hagfeldt, *Science* **2017**, *358*, 739.
[23] W. Lee, J. Lee, H. Yun, J. Kim, J. Park, C. Choi, D. C. Kim, H. Seo, H. Lee, J. W. Yu, W. B. Lee, D.-H. Kim, *Adv. Mater.* **2017**, *29*, 1702902.
[24] C. Y. Wu, Z. Wang, L. Liang, T. Gui, W. Zhong, R. C. Du, C. Xie, L. Wang, L. B. Luo, *Small* **2019**, *15*, 1900730.
[25] C. Cheng, C. Zhu, B. Huang, H. Zhang, H. Zhang, R. Chen, W. Pei, Q. Chen, H. Chen, *Adv. Mater. Technol.* **2019**, *4*, 1800729.
[26] Y. Liu, F. Li, C. Perumal Veeramalai, W. Chen, T. Guo, C. Wu, T. W. Kim, *ACS Appl. Mater. Interfaces* **2017**, *9*, 11662.
[27] Z. Gu, Z. Zhou, Z. Huang, K. Wang, Z. Cai, X. Hu, L. Li, M. Li, Y. S. Zhao, Y. Song, *Adv. Mater.* **2020**, *32*, 1908006.
[28] J.-U. Park, M. Hardy, S. J. Kang, K. Barton, K. Adair, D. K. Mukhopadhyay, C. Y. Lee, M. S. Strano, A. G. Alleyne, J. G. Georgiadis, P. M. Ferreira, J. A. Rogers, *Nat. Mater.* **2007**, *6*, 782.
[29] M. S. Onses, E. Sutanto, P. M. Ferreira, A. G. Alleyne, J. A. Rogers, *Small* **2015**, *11*, 4237.
[30] L. Chao, Y. Xia, B. Li, G. Xing, Y. Chen, W. Huang, *Chem* **2019**, *5*, 995.
[31] D. Huang, P. Xie, Z. Pan, H. Rao, X. Zhong, *J. Mater. Chem. A* **2019**, *7*, 22420.
[32] H. Li, N. Liu, Z. Shao, H. Li, L. Xiao, J. Bian, J. Li, Z. Tan, M. Zhu, Y. Duan, L. Gao, G. Niu, J. Tang, Y. Huang, Z. Yin, *J. Mater. Chem. C* **2019**, *7*, 14867.
[33] P. P. von Weimarn, *Chem. Rev.* **1925**, *2*, 217.
[34] F. T. L. Muniz, M. A. R. Miranda, C. Morilla dos Santos, J. M. Sasaki, *Acta Crystallogr., Sect. A: Found. Adv.* **2016**, *72*, 385.
[35] D. Liu, W. Zhou, H. Tang, P. Fu, Z. Ning, *Sci. China: Chem.* **2018**, *61*, 1278.
[36] J. Xiao, D. Attinger, presented at *Excerpt from the Proc. COMSOL Conf.*, Boston, MA, October **2010**.
[37] B. Peng, Z. Wang, P. K. L. Chan, *J. Mater. Chem. C* **2016**, *4*, 8628.
[38] W. Tian, H. Zhou, L. Li, *Small* **2017**, 13.